AIAA 90-0430
Transonic Navier-Stokes Solutions About a Complex High-Speed Accelerator Configuration

F. Ghaffari and B. Bates
ViGYAN Inc.
Hampton, VA
J. Luckring and J. Thomas
NASA-Langley
Hampton, VA

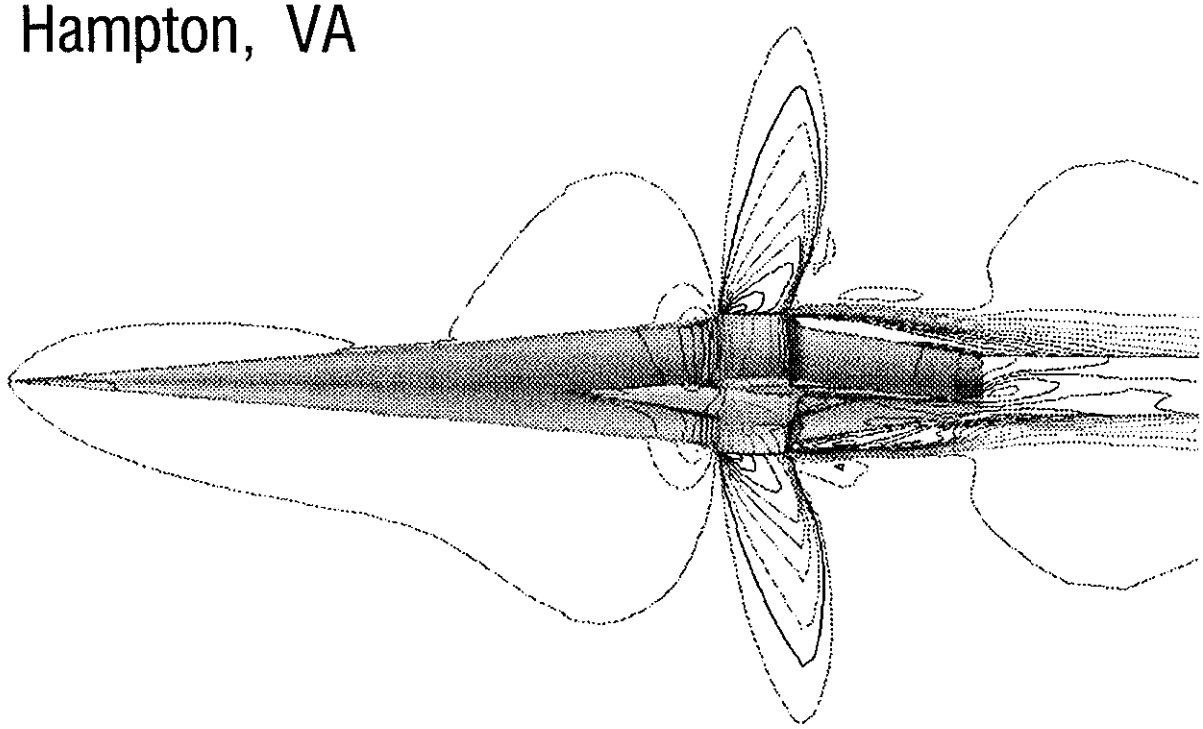

28th Aerospace Sciences Meeting
January 8-11, 1990/Reno, Nevada

For permission to copy or republish, contact the American Institute of Aeronautics and Astronautics
370 L'Enfant Promenade, S.W., Washington, D.C. 20024

Transonic Navier-Stokes Solutions about a Complex High-Speed Accelerator Configuration

Farhad Ghaffari†
ViGYAN, Inc.
James M. Luckring‡ , James L. Thomas§
NASA-Langley Research Center
Brent L. Bates‡
ViGYAN, Inc.

Abstract

Three-dimensional transonic viscous flow computations are presented for a generic high-speed accelerator model which includes wing, body, fillets, and a no-flow through engine nacelle. Solutions are obtained from an algorithm for the compressible Navier-Stokes equations which incorporates an upwind-biased, flux-vector-splitting approach along with longitudinally-patched grids. Results are presented for fully turbulent flow assumptions and include correlations with wind tunnel data. A good quantitative agreement for the forebody surface pressure distribution is achieved between computations and the available wind-tunnel measurements at $M_\infty = 0.9$. Furthermore, it is demonstrated that the flow is stagnating around the boattail region due to separation from the aft-engine cowl lip.

Nomenclature

a	speed of sound
C_L	lift coefficient, Lift/ $q_\infty S_{ref}$
C_p	pressure coefficient, $(p - p_\infty)/q_\infty$
C_p^*	critical pressure coefficient
c_p	specific heat at constant pressure
c_v	specific heat at constant volume
ℓ	total body length
E_o	total energy per unit volume
$\hat{F}, \hat{G}, \hat{H}$	flux vectors
h_o	total enthalpy, $(E_o + p)/\rho$
J	Jacobian of the coordinate transformation
k	conductivity, $c_p\mu/\ Pr$
M_∞	freestream Mach number
Pr	Prandtl number
$\hat{Q}$	state vector, $J^{-1}[\rho, \rho u, \rho v, \rho w, E_o]^T$
q	total velocity
q_∞	freestream dynamic pressure
R_ℓ	Reynolds number based on ℓ
S_{ref}	area of reference wing planform
u, v, w	body-axis Cartesian velocity components
v^*	wall-friction velocity, $\sqrt{\tau_w/\rho}$
x/ℓ	normalized longitudinal distance aft of nose
y^+	inner-law variable, yv^*/ν
α	angle of attack, degrees
$\beta,\ \delta$	residual parameters
γ	ratio of specific heats, c_p/c_v
μ	viscosity
ν	kinematic viscosity, μ/ρ
θ	azimuthal angle
ξ, η, ς	body-fitted coordinates
ρ	density
τ_w	wall shear stress

Introduction

The proposed National Aero-Space Plane (NASP) has revived interest in hypersonic flow research in the past few years, particularly, in the area of computer algorithm developments. The design of such a vehicle, inevitably, would rely heavily on Computational Fluid Dynamics (CFD), since the current ground test facilities are limited to lower speed regimes. Also, CFD results generally provide much more information about the flow structure and its detail mechanism than one can obtain experimentally.

The challenges associated with grid generation and surface definition along with a relatively large computational memory requirements hampers the applications of advanced CFD-code methodologies to complex aircraft configurations. None the less, recent progress has been shown for several cases including subsonic inviscid flow computations about the complete F-14 configuration[1] as well as transonic viscous flow about the F-16A[2]. In addition, viscous flow computations about the ascent configuration of the space shuttle[3] have shown good agreement with flight data at subsonic, transonic, and supersonic speeds. Most recently, three-dimensional viscous flow computations about the F/A-18 forebody-LEX configuration[4] have

†Research Engineer, Senior member AIAA
‡Research Engineer, Member AIAA
§Senior Research Scientist, Associate Fellow AIAA

This paper is declared a work of the U.S. Government and is not subject to copyright protection in the United States.

demonstrated good correlation with the experimental wind-tunnel data as well as flight test results. Prior computations for generic NASP type configurations have demonstrated the applicability of Navier-Stokes methodology to transonic[5] as well as hypersonic[6] flow with Mach numbers exceeding 20.

The present investigation is directed toward applying an extended version of an implicit Navier-Stokes algorithm[7-10] to a generic high-speed accelerator model at $M_\infty = 0.9$, $R_\ell \approx 30 \times 10^6$, $\alpha = 2°$. At these conditions the flow is assumed to be fully turbulent, hence only turbulent computations are performed. The algorithm permits longitudinally-blocked grids which are necessary for accurately modeling the subject configuration. The accelerator geometry has been selected for this study primarily due to the availability of current transonic wind-tunnel data[11,12] as well as a growing interests at NASA in utilizing the state-of-the-art CFD codes to analyze the flow about the NASP type configuration in all speed regimes.

Governing Equations

The governing equations as well as computational method for the present investigation have been published many times in the open literature[7-10] as they have evolved. The flow is presumed to be governed by the unsteady Reynolds-averaged Navier-Stokes equations which are written in a body-fitted coordinate system. They are written in a usual conservation-law form as

$$\hat{Q}_{,t} + (\hat{F} - \hat{F}_v)_{,\xi} + (\hat{G} - \hat{G}_v)_{,\eta} + (\hat{H} - \hat{H}_v)_{,\zeta} = 0$$

Here the subscripts with a comma denote partial differentiation, the subscript v identifies the viscous terms, and the superscript $\hat{}$ indicates scaling with respect to the Jacobian of the coordinate transformation. With the ideal gas assumption, the pressure and total enthalpy can be expressed as

$$p = (\gamma - 1)(E_o - \frac{1}{2}\rho q^2) \quad ; \quad h_o = \frac{\gamma}{\gamma - 1}\frac{p}{\rho} + \frac{1}{2}q^2$$

For the present study, the thin layer approximation to the governing equations is invoked (i.e., $\hat{F}_v = \hat{G}_v = 0$) thus accounting for viscous flux terms only in the ζ direction (normal to the body). Detail for these terms are included in Appendix 1.

Turbulence effects are accounted for through the notion of an eddy viscosity and eddy conductivity:

$$\mu = \mu_\ell + \mu_t = \mu_\ell (1 + \mu_t/\mu_\ell)$$

$$k = k_\ell + k_t = k_\ell (1 + k_t/k_\ell) = \frac{c_p \mu_\ell}{Pr_\ell}\left(1 + \frac{\mu_t Pr_\ell}{\mu_\ell Pr_t}\right)$$

Here the subscripts ℓ and t denote laminar and turbulent, respectively. The algebraic turbulence model developed by Baldwin and Lomax[13] is used to evaluate appropriate turbulence quantities. For separated flow regions, the notions of Degani and Schiff[14] are drawn upon to determine proper turbulence length scales.

Computational Method

Discretization of the governing equations results in a consistent approximation to the conservation laws in integral form

$$\frac{\partial}{\partial t}\int\int\int \hat{Q} dV + \int\int \vec{\hat{f}} \cdot \hat{n} dS = 0$$

where the time rate of change of the state vector $\hat{Q}$ within a cell is balanced by the net flux $\vec{\hat{f}}$ across the cell surface. The convective and the pressure terms arising in the flux quantities are represented using an upwind biased algorithm, with either the flux-vector-splitting approach of van Leer[15] or the flux-difference-splitting approach of Roe[16]. Both approaches rely on a reconstruction of primitive variable data at the cell-centers to the cell-interfaces; the reconstruction is monotone to prevent oscillations near discontinuities, such as shocks, and is third- order accurate in the special case of one-dimensional flows. The shear stress and the heat transfer terms are centerally differenced so that the resulting algorithm is spatially second-order accurate. Solutions are advanced in time with a spatially-split approximate factorization method which, in general, solves a series of block 5x5 tridiagonal matrices to advance the solution to a new time level. For the flux-difference splitting scheme, the implicit terms are diagonalized, leading to a series of scalar tridiagonal inversions.

In the present computations, attempts were made initially to use flux-difference splitting with third-order accuracy. However, due to convergence difficulties the alternative flux-vector-splitting approach was invoked. Prior results[17] have shown the van Leer scheme to diffuse boundary layers, particularly when utilized with first-order accuracy and/or with sparse grid resolution. This limitation was overcome in the present work by utilizing the van Leer scheme with third-order accuracy and by performing the computations with a sufficiently dense mesh. Salient aspects of the van Leer formulation are discussed in Appendix 2.

Information is exchanged between the longitudinal blocks using the patching algorithm described by Thomas, et. al[10]. At the interface between the two blocks, the dependent variables at the cell centers of each zone are interpolated across the coincident interface boundary assuming a biquadratic variation across each cell of the opposing zone. The interpolation is second order accurate and conserves the mass, momentum,

and energy across the zonal interface only to within the truncation error of the discrete solution.

Experimental Models

There were two accelerator models tested in the Langley's 16-foot transonic wind-tunnel. The first model was a sting mounted model with an open inlet and exhaust faces (i.e., flow-through). This model, called the "forebody" model, was intended to only provide experimental pressure data on the forebody. The second model, called the "propulsion" model, had a faired over (closed) inlet and open exhaust face to allow for the simulation of propulsion effects. This model was mounted on a strut which housed some of the exhaust jet-flow propulsion apparatus. The experiment was designed to obtain experimental pressure measurements on the boattail region for various exit mass-fluxes including zero (i.e., a jet-off case).

Numerical Model Representation

The surface grid definition is obtained from an analytical representation of the configuration. The complete surface representation of the configuration along with various longitudinal cuts are shown in Fig. 1. The body of the configuration consists of a 5° half-angle right-circular cone and a 9° boattail frustum that are connected with a cylinder. A nacelle is wrapped around the cylindrical part of the body. The configuration incorporates wing-fillets on both the starboard as well as the port side of the body. The front engine wing-fillet blends into the nacelle cowl at a longitudinal station between stations C and D (Fig. 1). The aft-engine wing-fillet merges smoothly into the wing upper and lower surfaces, at a longitudinal station between stations E and F. The configuration included a 70° swept sharp delta wing with a span of $0.11 \times \ell$. The wing had a 4% thick biconvex airfoil and was mounted at 3° incidence on the combinations of front and aft-engine fillets as well as the nacelle.

The inlet face is faired over similar to the tested wind-tunnel propulsion model. Since the effects of propulsion are not included in the present computations, the exhaust face was also faired over with a 45° ramp. This fairing eliminates the problem of having a surface discontinuity at the exit plane, where there needs to be a longitudinal patching station of two blocks from a geometrical consideration (i.e., start of the aft-fillet). The surface geometry is defined with a total of 5,400 grid points at 88 longitudinal stations along the body.

The field grid is divided into eight longitudinal blocks, each representing a local geometrical complexity of the configuration. The forebody block is generated with a C-O grid topology thus resolving the nose radius and extending to the upstream inflow boundary. Figure 2 shows the forebody grids on the surface, plane of symmetry, as well as the base section. In this figure, the radial extent of the grid has been truncated for clarity. The three-dimensional grid for the remaining blocks are constructed from two-dimensional O-type cross flow grids which are longitudinally stacked, constituting an H-O topology. Figure 3 illustrates a farfield as well as a nearfield view of complete grid about the accelerator configuration in the plane of symmetry. The grid lines in the radial direction are plotted for every fourth point for clarity. The grid dimensions as well as the mesh topology for each corresponding block are listed in Table 1.

Block	x	θ	r	*Points*	*Top*
1	29	31	65	58435	C-O
2	12	59	65	46020	H-O
3	12	91	65	70980	H-O
4	9	79	65	46215	H-O
5	13	91	65	76895	H-O
6	9	75	65	43875	H-O
7	4	31	65	8060	H-O
8	11	31	65	22165	H-O

Table 1. Grid dimensions and topology.

The upstream, downstream, and the radial extent of the flowfield grid is about one configuration body length which corresponds to 13.5 times the maximum body diameter. Block 8 is the downstream extention of the grid and has 11 longitudinal stations. All blocks have 65 points in the radial direction and the circumferential number of grid points vary from block to block depending on the complexity of the local cross-sectional geometry. Longitudinally, the grids are clustered near each geometrical break such as a station where the wing starts or terminates. There are approximately 373,000 grid points used to represent the entire flowfield domain.

The crossflow grids are generated using established transfinite interpolation techniques[18,19] with a method applicable to slender shapes[4,6]. The flowfield grid is generated with sufficient normal clustering near the surface to adequately resolve the laminar sublayer of the turbulent boundary layer flow at the subject wind-tunnel freestream conditions ($M_\infty = 0.9$, $R_\ell \approx 30 \times 10^6$, $\alpha = 2°$). This grid produced an average normal cell-center size next to the wall of approximately $10^{-5}\ell$ which corresponded to $y^+ \approx 3$ for the turbulent computations; a laminar sublayer generally extends out to $y^+ \approx 8.5$. Fig. 4 illustrates the nearfield view of a typical configuration cross section as well as the grid resolution in the vicinity of the fillet-body and fillet-wing

juncture. This figure illustrates the challenge that is associated with generating a single O-type grid around such complex cross section with various break points in the surface geometry.

Results and Discussion

Results are presented first for general flow features. This is followed with a discussion of some convergence attributes of the computed results. Finally, a comparison between the computed surface pressures and the available experimental data are presented on the forebody as well as boattail region.

Solution Attributes

Mach contours on the surface and in the configuration plane of symmetry at the subject wind-tunnel flow conditions are shown in Fig. 5. The sonic line is highlighted with a white contour line in the plane of symmetry to highlight the supersonic flow region. The magnitudes associated with contour quantities are displayed with a color bar. This figure indicates that after a basically subsonic forebody, the flow accelerates supersonically over the faired-over inlet, follows with a mild compression on the engine cowl and it subsequently shocks down at the aft-engine cowl-lip. The presence of the shock along with the slanted exhaust-face produces a large adverse pressure gradient which causes the flow to separate at the exhaust cowl-lip and subsequently envelop the entire boattail region. Note that the Mach contours smoothly cross over the many block interfaces. Cross-flow Mach contours are shown in Fig. 6 for various planes along the length of the configuration. This figure illustrates the radial extent of the supersonic zone in two cross-flow planes: one on the nacelle and the other slightly aft of it cutting through the shock. In addition, the complex flow structure in the separated boattail region is well depicted in the last two cross-flow planes. It should be noted that the propulsion effects (i.e., either a simple flow-through or the actual engine simulation) are expected to have a significant influence in the supersonic region as well as the separated flow in the boattail region.

The total pressure contours in various cross-flow planes along the body as well as in the plane of symmetry are shown in Fig. 7(a). The flow appears to be primarily attached on the forebody. Also, the losses that are associated with viscous flow are well depicted in the separated boattail region. Figure 7(b) shows a closeup view of the total pressure contours to highlight the smaller separated flow structures that exist on the engine cowl as well as the wing upper surface. The separated flow on the cowl is associated with the fillet-body juncture flow that is spilling over the cowl on its lower surface and, to a lesser degree, on its upper surface. The small flow structure on the wing upper surface is evidence of a leading-edge bubble type separation. The flow intensity at the center of this separated flow is reduced significantly as it passes through the shock which is sitting at the aft-engine cowl-lip and extended circumferentially over onto the wing surface.

The computed streamlines on the configuration upper surface as well as in the plane of symmetry are presented in Fig. 8. This figure clearly shows the abrupt change in the streamline pattern on the wing upper surface near the aft-engine cowl-lip that signifies the presence of the shock. The turning of the surface flow streamlines is primarily due to the diminished axial velocity component of the flow. Consequently, in the wing tip region, the streamlines appear to go around the wing leading edge to the lower surface. Fig. 8 also shows the very complex surface flow pattern that is associated with the low speed flow in the boattail region; this pattern appears to indicate a whorl.

Convergence Characteristics

The flow computations were performed on the NAS Cray 2, located at NASA-Ames. On this machine, the algorithm requires approximately 50 μ seconds per grid point per cycle. The present numerical results for the $\alpha = 2^\circ$ were obtained in nominally 4815 cycles which required about 25 hours of computer time. This number of cycles was sufficient to reduce the residuals by three orders of magnitude and limit the oscillations in C_L to $\approx \pm.005$ (Fig. 9). The computations were performed without the use of mesh sequencing or multigrid iteration.

The salient features of the flow were examined during the course of the convergence process. It was found that the position of the shock and the shape of the supersonic pocket was apparently established within approximately the first 2000 cycles. The loss in C_L, shown in Fig. 9, for $1500 \leq iterations \leq 2000$ is primarily associated with the formation of separated flow in the boattail region. Subsequent to establishing the shock structure ($iteration \approx 2000$), changes in this separated flow region result in a further loss of lift for the next ≈ 1000 cycles after which changes in lift become small. The separated flow region appears to exhibit certain unsteady flow characteristics which are associated with the downstream convection of flow quantities from the exhaust face. There are reasons to believe that this separated region is the primary cause of the oscillations in the lift as well as the residual magnitude for the last 1500 cycles (see Fig. 9).

To examine this conjecture, the individual block *rms* residuals (β_n) are appropriately weighted by the

fraction of grid points in each block,

$$\delta_n^2 = \left[\frac{np_n}{np_{total}}\right](\beta_n)^2$$

where

$$(\beta_n) = \sqrt{\frac{1}{np_n}\sum_{i=1}^{i=np_n} residual_i^2}$$

In the above equations, $residual_i$ refers to the residual in cell i and np_n refers to the number of points for block n. The total rms residual for the complete configuration can now be obtained from

$$residual_{total} = \sqrt{\sum_{n=1}^{N} \delta_n^2}$$

where N is the total number of blocks. The block residual distribution is presented in Fig. 10 for four different levels of iterations. This figure shows that the incremental local residual for blocks 5, 6, and 7 are relatively more dominant than the corresponding residuals for the upstream blocks 1 through 4. The separation in the boattail region is mainly responsible for the large local residuals as well as their oscillatory behavior with number of iterations. This separation also appears to be the principal cause for the excessive total number of iterations performed to achieve the present results. Note that the local block-residual for the first 4-blocks are not changing much by advancing the solution from 2455 to 4815 cycles; the flow on the forebody appears to have setup within the first 2455 cycles.

The surface pressure sensitivity on the developping solution was also examined at three iteration levels. Figure 11 illustrates longitudinal pressure distributions on the accelerator forebody at five conical rays; $\theta = 0°$ corresponds to the windward and $\theta = 180°$ to the leeward side of the configuration plane of symmetry. This figure also shows a schematic side view of the computational accelerator body to highlight the longitudinal extent of the forebody. As discussed previously in the solution attributes, the forebody appears to exhibit a fairly benign flow condition with the expected flow compression in the vicinity of the inlet face. It is also evident that the computed surface pressures are less sensitive to the last 1310 cycles beyond 3505.

The boattail surface pressure sensitivity in the plane of symmetry for the same number of cycles are shown in Fig. 12(a). This is basically the continuation of the forebody pressures shown in the previous figure onto the engine-cowl and the boattail region in the plane of symmetry. The flow accelerates over the faired-over inlet supersonically ($C_p^* \approx -0.2$) and then it goes through a mild compression over the engine cowl and subsequently shocks down at the aft-engine cowl-lip. Note that the supersonic region, as well as the shock strength and its position are well established with $\approx$ 2800 cycles. However, the pressures on the boattail region appear to be somewhat sensitive to those number of cycles examined.

The circumferential pressure distribution at two stations, one ahead of the shock ($x/l = 0.768$) and the other aft of the shock ($x/l = 0.828$), are presented in Fig. 12(b), along with their corresponding geometrical cross-section. The left part of the figure shows the variation of pressures as a function of azimuthal angle θ on the body. The right part of the figure shows the pressures on the wing ($x/l = 0.768$) and wing as well as the fillets ($x/l = 0.828$) as a function of the exposed wing or wing-fillet semispan, respectively. Notice these plots have scales that are three times as fine as the figures on the left. The pressure distribution at the station ahead of the shock appears to be insensitive to the number of cycles, particularly on the wing. Furthermore, the effects of the separated flow emitted from the fillet-body juncture over the engine cowl surface ($x/l = 0.768$) are well evident at $\theta \approx 60°$ (i.e. lower surface) and $\theta \approx 100°$ (i.e. upper surface). As discussed earlier, the pressures at the station aft of the shock experiences some sensitivity to the number of cycles. The pressures on the wing clearly show the loss of the wing leading-edge suction after passing through the shock.

In summary, the results from the surface pressure sensitivity study indicate that the flow on the forebody appears to had been well established within the first 3500 cycles. These results also reveal that the supersonic pocket over the engine cowl as well as the shock position and its strength were fully developed at about 2800 iterations. Furthermore, the flow in the separated boattail region were most sensitive to the number of cycles. Note that these results complement the findings discussed earlier from the residual-history point of view.

Data Comparison

The computed static pressure coefficients on the forebody are compared with the experimentally measured data[11,12] in Fig. 13. The figure shows the comparison at five different conical rays from windward ($\theta = 0°$) to leeward side ($\theta = 180°$) in 45° increments. A schematic side view of the accelerator body for both the wind-tunnel model as well as the computational model are also shown to highlight the major geometrical differences that exist between them. As described previously, the experimental forebody pressures were obtained on the same model but only for flow through inlet conditions whereas the numerical model had the

faired over inlet and exhaust face. The longitudinal extent of the forebody covers approximately 70% of the configuration total body length. This figure reveals a good correlation between experimental data and the computed results up to $x/\ell \approx 0.4$. The discrepancies between theory and data in x/ℓ range of 0.4 - 0.7 are mainly due to the differences in inlet flow conditions. The faired over inlet produces additional compression which results in a more positive pressures as indicated in the computed results of Fig. 13.

The computed pressure coefficient on the boattail are plotted against the measured data in Fig. 14(a), along the configuration plane of symmetry. This figure also shows a schematic side view of the experimental as well as computational model to illustrate the major differences that exist in the exhaust face with regard to the geometry and the flow condition. The data correspond to the experimental condition of zero-mass flux across the exit. This figure reveals a fairly good correlation between theory and experiment. The discrepancies in the neighborhood of the exit could well be due to geometrical differences at the exit face and/or the back pressure effects from the open exhaust face in the experiment.

The circumferential theoretical and the experimental data for two longitudinal stations on the boattail region are shown in Fig. 14(b). The first station is located slightly aft of the shock ($x/l = 0.828$) and the other further downstream ($x/l = 0.961$). Notice that the scales have been magnified to bring out the differences. At $x/l = 0.828$ there are some disagreements between theory and experiment although the trend appears to have been better predicted. At $x/l = 0.961$ the agreement between theory and experiment is quite good. In general, the flow structure in the boattail region is very complex, and the correlations that have been achieved there are perhaps better than might have been expected.

Concluding Remarks

Three-dimensional transonic viscous flow computations for a complex high-speed accelerator are presented with fully turbulent flow assumptions. Good correlation between experimental static pressures and computational results on the forebody are disclosed. The computed results show a large supersonic pocket over the nacelle surface with a shock at the aft-engine cowl-lip. The presence of the shock as well as the slanted exhaust face cause the flow to separate into a very complex flow structure envelopping the entire boattail region. None the less, some quantitative comparisons have been made between theory and experiment in the boattail region.

Appendix 1 - Governing Equations

The inviscid flux terms from the governing equation are defined as follows:

$$\hat{Q} = \frac{1}{J}\begin{Bmatrix} \rho \\ \rho u \\ \rho v \\ \rho w \\ E_o \end{Bmatrix} \quad ; \quad \hat{F} = \frac{1}{J}\begin{Bmatrix} \rho U \\ \rho U u + \xi_{,x} p \\ \rho U v + \xi_{,y} p \\ \rho U w + \xi_{,z} p \\ (E_o + p)U \end{Bmatrix}$$

$$\hat{G} = \frac{1}{J}\begin{Bmatrix} \rho V \\ \rho V u + \eta_{,x} p \\ \rho V v + \eta_{,y} p \\ \rho V w + \eta_{,z} p \\ (E_o + p)V \end{Bmatrix} \quad ; \quad \hat{H} = \frac{1}{J}\begin{Bmatrix} \rho W \\ \rho W u + \varsigma_{,x} p \\ \rho W v + \varsigma_{,y} p \\ \rho W w + \varsigma_{,z} p \\ (E_o + p)W \end{Bmatrix}$$

The contravariant velocity components in these equations are given by:

$$\begin{Bmatrix} U \\ V \\ W \end{Bmatrix} = \begin{Bmatrix} \xi_{,x} u + \xi_{,y} v + \xi_{,z} w \\ \eta_{,x} u + \eta_{,y} v + \eta_{,z} w \\ \varsigma_{,x} u + \varsigma_{,y} v + \varsigma_{,z} w \end{Bmatrix}$$

The thin layer viscous flux terms from the governing equation are defined as follows:

$$\hat{H}_v = \frac{M_\infty \mu}{R_\ell J}\begin{Bmatrix} 0 \\ u_{,\varsigma}\phi_{\varsigma 1} + \varsigma_{,x}\phi_{\varsigma 2} \\ v_{,\varsigma}\phi_{\varsigma 1} + \varsigma_{,y}\phi_{\varsigma 2} \\ w_{,\varsigma}\phi_{\varsigma 1} + \varsigma_{,z}\phi_{\varsigma 2} \\ \left((\frac{q^2}{2})_{,\varsigma} + \frac{T_{,\varsigma}}{Pr(\gamma-1)}\right)\phi_{\varsigma 1} + W\phi_{\varsigma 2} \end{Bmatrix}$$

where

$$\{\phi_{\varsigma 1}\} = \{(\varsigma_{,x})^2 + (\varsigma_{,y})^2 + (\varsigma_{,z})^2\}$$

$$\{\phi_{\varsigma 2}\} = \frac{1}{3}\{u_{,\varsigma}\varsigma_{,x} + v_{,\varsigma}\varsigma_{,y} + w_{,\varsigma}\varsigma_{,z}\}$$

The transformation metrics are:

$$\begin{bmatrix} \xi_{,x} & \eta_{,x} & \varsigma_{,x} \\ \xi_{,y} & \eta_{,y} & \varsigma_{,y} \\ \xi_{,z} & \eta_{,z} & \varsigma_{,z} \end{bmatrix} =$$

$$J\begin{bmatrix} y_{,\eta}z_{,\varsigma} - z_{,\eta}y_{,\varsigma} & z_{,\xi}y_{,\varsigma} - y_{,\xi}z_{,\varsigma} & y_{,\xi}z_{,\eta} - z_{,\xi}y_{,\eta} \\ z_{,\eta}x_{,\varsigma} - x_{,\eta}z_{,\varsigma} & x_{,\xi}z_{,\varsigma} - z_{,\xi}x_{,\varsigma} & z_{,\xi}x_{,\eta} - x_{,\xi}z_{,\eta} \\ x_{,\eta}y_{,\varsigma} - y_{,\eta}x_{,\varsigma} & y_{,\xi}x_{,\varsigma} - x_{,\xi}y_{,\varsigma} & x_{,\xi}y_{,\eta} - y_{,\xi}x_{,\eta} \end{bmatrix}$$

and the Jacobian of the transformation is given by:

$$J^{-1} = x_{,\xi}(y_{,\eta}z_{,\varsigma} - z_{,\eta}y_{,\varsigma}) - y_{,\xi}(x_{,\eta}z_{,\varsigma} - z_{,\eta}x_{,\varsigma}) + z_{,\xi}(x_{,\eta}y_{,\varsigma} - y_{,\eta}x_{,\varsigma})$$

Appendix 2 - Upwind Algorithm

Generalized convective and pressure fluxes are split into forward and backward contributions and differenced according to the van Leer flux-vector splitting scheme. Using the ξ−direction as an example

$$\begin{aligned}(\delta\hat{F}/\delta\xi)_i &= [\delta_\xi^- \hat{F}^+ + \delta_\xi^+ \hat{F}^-]_i \\ &= [\hat{F}^+(Q^-) + \hat{F}^-(Q^+)]_{i+1/2} \\ &\quad - [\hat{F}^+(Q^-) + \hat{F}^-(Q^+)]_{i-1/2}\end{aligned}$$

where $\delta\xi = 1$ and $\hat{F}^+(Q^-)_{i+1/2}$ denotes a forward flux evaluated with an upwind biased interpolated state variables.

The flux is split according to the contravariant Mach number, $M_\xi = \bar{u}/a$, where

$$\bar{u} \equiv U/ \mid grad(\xi) \mid$$

For supersonic flow $\mid M_\xi \mid \geq 1$ and

$$\begin{aligned}\hat{F}^+ &= \hat{F},\ \hat{F}^- = 0\ ;\quad M_\xi \geq +1 \\ \hat{F}^- &= \hat{F},\ \hat{F}^+ = 0\ ;\quad M_\xi \leq -1\end{aligned}$$

For subsonic flow $\mid M_\xi \mid < 1$ and

$$\hat{F}^\pm = \frac{f^\pm_{mass} \mid grad(\xi) \mid}{J} \begin{Bmatrix} 1 \\ \hat{\xi}_{,x}(-\bar{u} \pm 2a)/\gamma + u \\ \hat{\xi}_{,y}(-\bar{u} \pm 2a)/\gamma + v \\ \hat{\xi}_{,z}(-\bar{u} \pm 2a)/\gamma + w \\ f^\pm_{energy} \end{Bmatrix}$$

where

$$f^\pm_{mass} = \pm\rho a(M_\xi \pm 1)^2/4$$

$$f^\pm_{energy} = [-(\gamma-1)\bar{u}^2 \pm 2(\gamma-1)\bar{u}a + 2a^2]/(\gamma^2-1) + q^2/2$$

and

$$[\hat{\xi}_{,x}, \hat{\xi}_{,y}, \hat{\xi}_{,z}]^T = [\xi_{,x}, \xi_{,y}, \xi_{,z}]^T / \mid grad(\xi) \mid$$

State variables at the cell interfaces are formed from interpolation of the primitive variables vector $q \equiv [\rho, u, v, w, p]^T$ by the one-parameter family

$$(q^-)_{i+1/2} = q_i + 1/4[(1-\kappa)\overline{\nabla q}_i + (1+\kappa)\overline{\Delta q}_i]$$

$$(q^+)_{i+1/2} = q_{i+1} - 1/4[(1+\kappa)\overline{\nabla q}_{i+1} + (1-\kappa)\overline{\Delta q}_{i+1}]$$

where the backward and forward differences are expressed respectively with a typical *minmod* limiter as

$$\overline{\nabla q} = minmod[\nabla q, B \triangle q]$$

$$\overline{\Delta q} = minmod[\Delta q, B \nabla q]$$

with

$$\begin{aligned}minmod(x, y) &\equiv sign(x)\times \\ &\quad max\left[0, min\big(x\ sign(y), y\ sign(x)\big)\right]\end{aligned}$$

Here B is a parameter which controls the maximum allowable range of successive gradients before limiting is applied. It is defined in terms of κ

$$B \equiv (3-\kappa)/(1-\kappa)$$

and $\kappa = 1/3$ for third-order accuracy in the special case of one-dimensional flow.

Acknowledgments

NASA-Langley Research Center sponsored the work of the 1st and 4th authors under NASA Contract No. NAS1-18585.

References

[1] Szema, K. Y.; Chakravarthy, S. R.; Bihari, B. L.: F-14 Flow Field Simulation. AIAA Paper No. 89-0642.

[2] Flores, J.; and Chaderjian, N. M.: The Numerical Simulation of Transonic Separated Flow About the Complete F-16A. AIAA Paper No. 88-2506, 1988.

[3] Buning, P. G.; Chiu, I. T.; Obayashi, S.; Rizk, Y. M.; and Steger, J. L.: Numerical Simulation of the Integrated Space Shuttle Vehicle in Ascent. AIAA Paper No. 88-4359, 1988.

[4] Ghaffari, F.; Luckring, J. M.; Thomas, J. L.; and Bates B. L.: Navier-Stokes Solutions about the F/A-18 Forebody-LEX Configuration. AIAA Paper No. 89-0338, 1989.

[5] Shrewsbery, G., D; Vadyak, J.; Schuster, D. M.; and Smith, M.,J.: Computation of Aircraft Component Flow Fields at Transonic Mach Numbers Using a Three-Dimensional Navier-Stokes Algorithm. NASA CP-3020, Vol. I,

[6] Richardson, P. F.; and Morrison, J. H.: Displacement Surface Calculations for a Hypersonic Aircraft. AIAA Paper No. 87-1190, 1987.

[7] Thomas, J. L.; and Newsome, R. W.: Navier-Stokes Computations of Lee-Side Flows over Delta Wings. AIAA Paper No. 86-1049, 1986.

[8] Thomas, J. L.; Taylor, S. L.; and Anderson, W. K.: Navier-Stokes Computations of Vortical Flows Over Low Aspect Ratio Wings. AIAA Paper No. 87-0207, 1987.

[9] Vatsa, V. N.; Thomas, J. L., and Wedan, B. W.: Navier-Stokes Computations of Prolate Spheroids at Angle of Attack. AIAA Paper No. 87-2627-CP, 1987.

[10] Thomas, J. L.; Walters, R. W.; Taekyu R.; Ghaffari, F.; Weston, R. P.; and Luckring, J. M.: A Patched Grid Algorithm for Complex Configurations Directed Towards the F-18 Aircraft. AIAA Paper No. 89-0121, 1989.

[11] Henderson, W. P., Lamb, M., and Bennet, B. D.: Aerodynamic Characteristics of a Powered Accelerator Model at Transonic Speeds (U). Paper-Number 85, Presented at the Fifth National Aero-Space Plane Technology Symposium, Monterey, Cal., Oct. 18-20, 1988.

[12] Henderson, W. P., and Bennet, B. D.: Forebody Pressure Distributions on a Conical Aerospace Plane Concept at Mach Numbers From 0.4 to 1.20 (U). NASP TM-1078, Aug. 1989.

[13] Baldwin, B. S.; and Lomax, H.: Thin Layer Approximation and Algebraic Model for Separated Turbulent Flows. AIAA Paper No. 78-257, 1978.

[14] Degani, D.; and Schiff, L. B.: Computation of Supersonic Viscous Flows Around Pointed Bodies at Large Incidence. AIAA Paper No. 83-0034, 1983.

[15] van Leer, B.: Flux-Vector Splitting for the Euler Equations. ICASE Report No. 82-30, Sep. 1982.

[16] Roe, P. L.: Characteristic Based Schemes for the Euler Equations. Annual Review of Fluid Mechanics, 1986, pp. 337-365.

[17] van Leer, B.; Thomas, J. L.; Roe, P. L.; and Newsome, R. W.: A Comparison of Numerical Flux Formulas for the Euler and Navier-Stokes Equations. AIAA Paper No. 87-1104-CP, 1987.

[18] Eriksson, L. E.: Practical Three-Dimensional Mesh Generation Using Transfinite Interpolation. Journal of Fluid Mechanics, Vol. 148, 1984, pp. 45-78.

[19] Smith, R. E.: Algebraic Grid Generation. Numerical Grid Generation, Elsevier, N.Y., 1982, pp. 137-168.

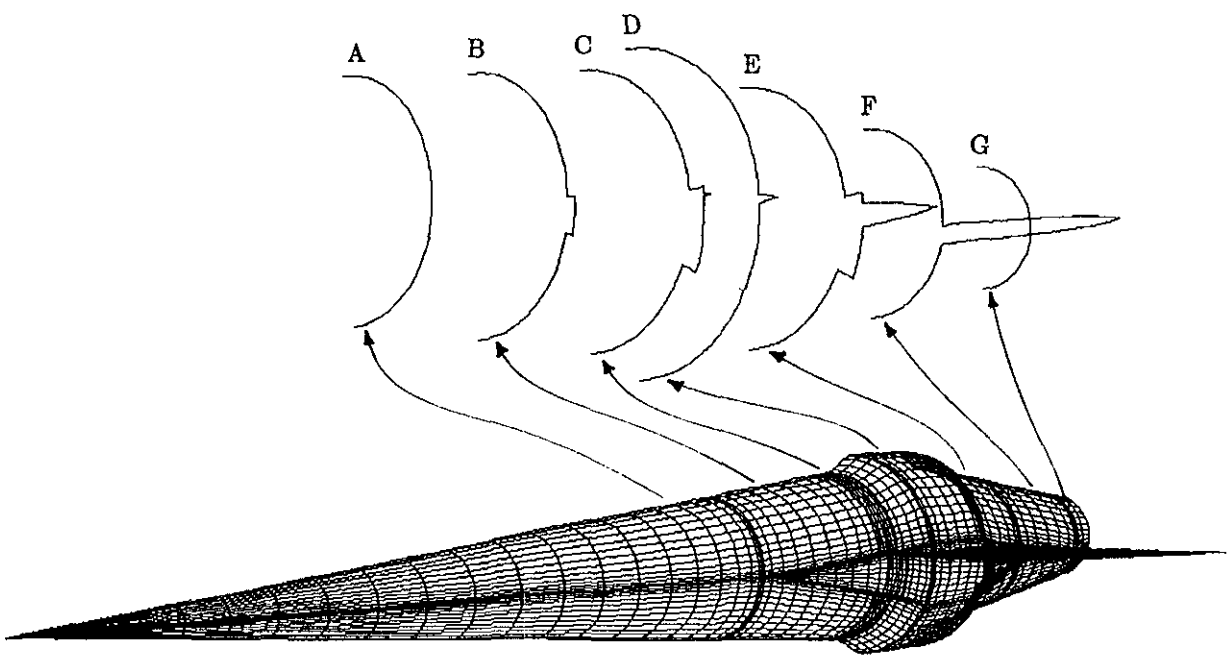

Figure 1.- Accelerator surface and cross-sectional grid.

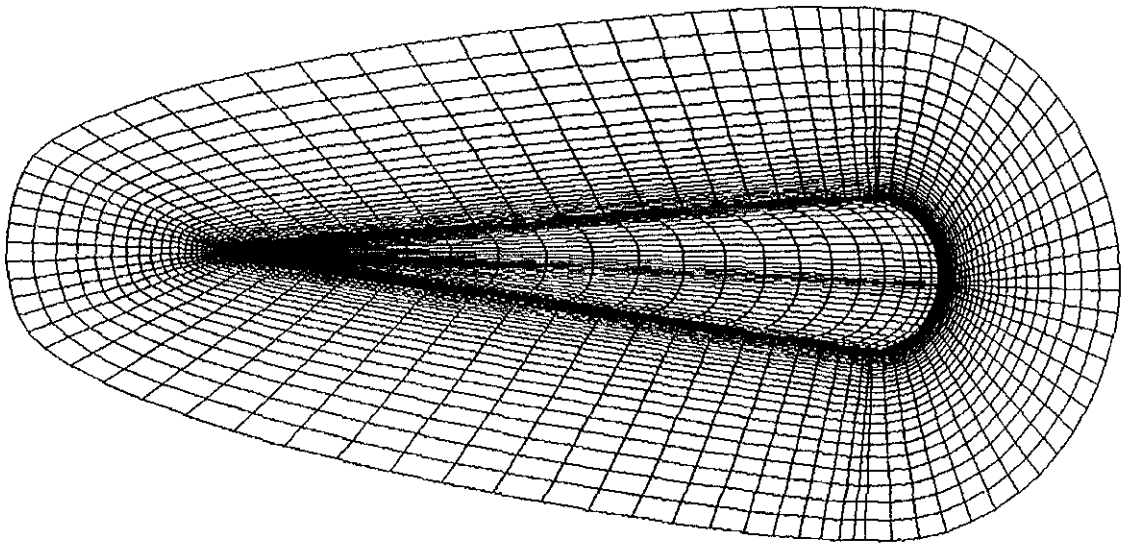

Figure 2.- Accelerator forebody C-O grid.

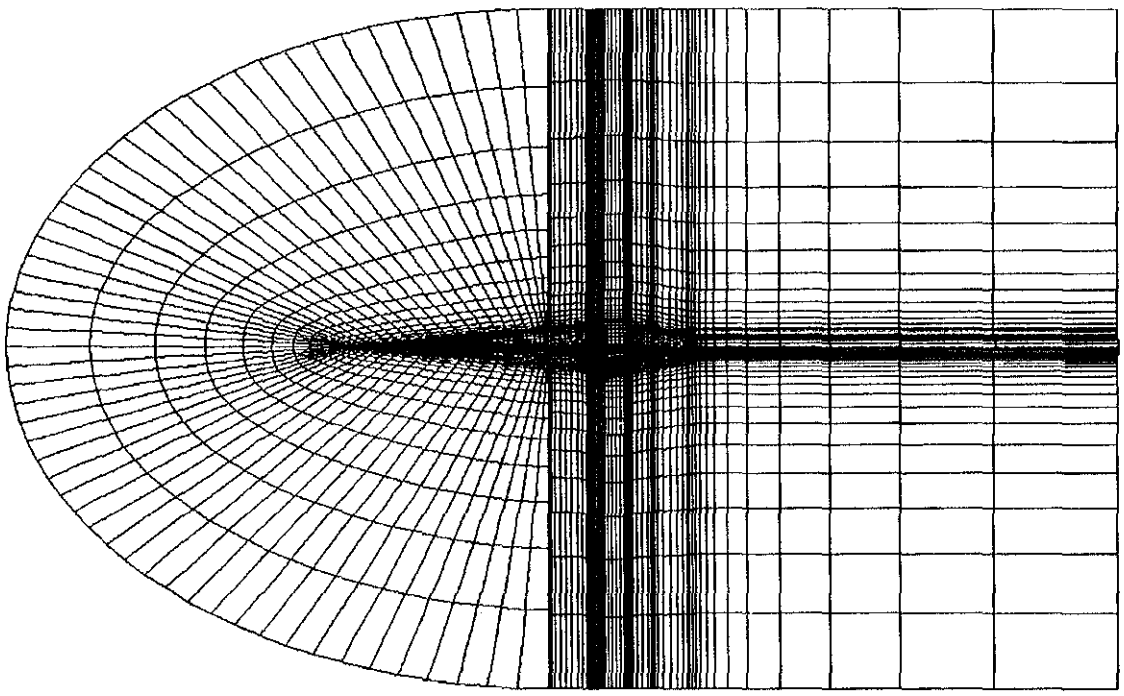

(a) Farfield.

Figure 3.- Blocking strategy for the accelerator configuration.

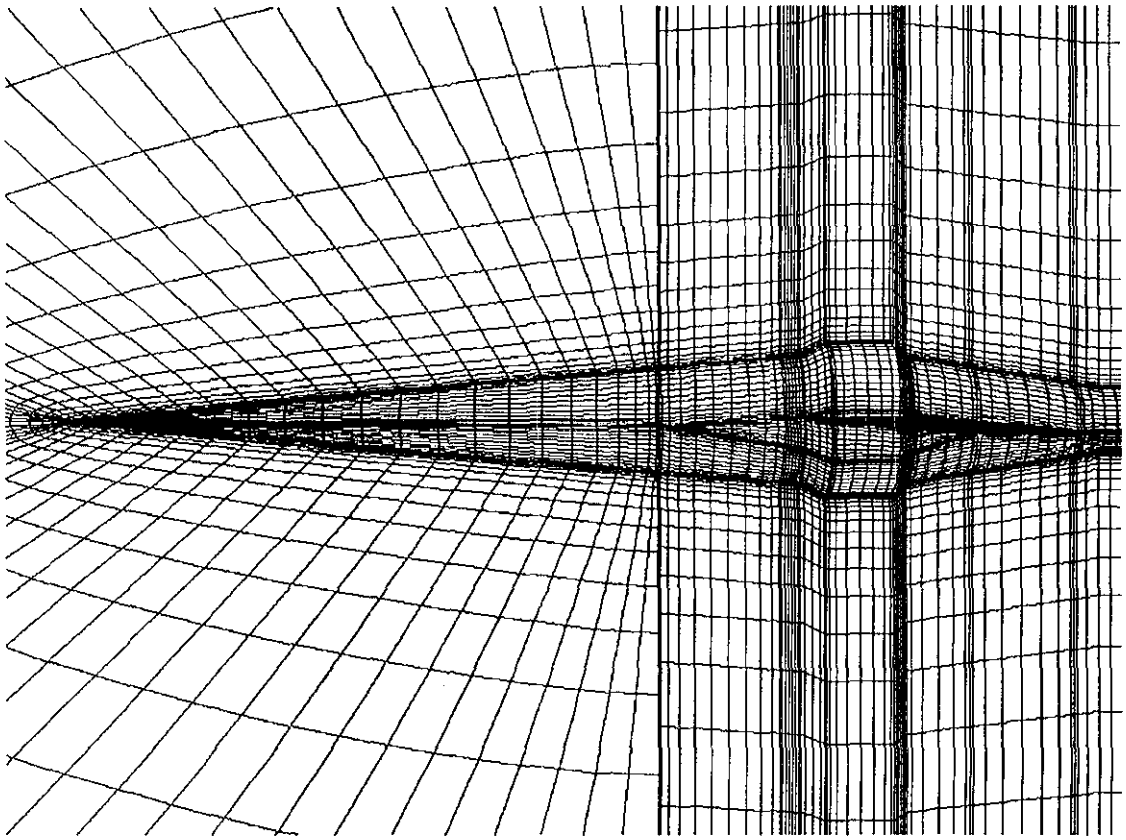

(b) Nearfield.

Figure 3.- Concluded.

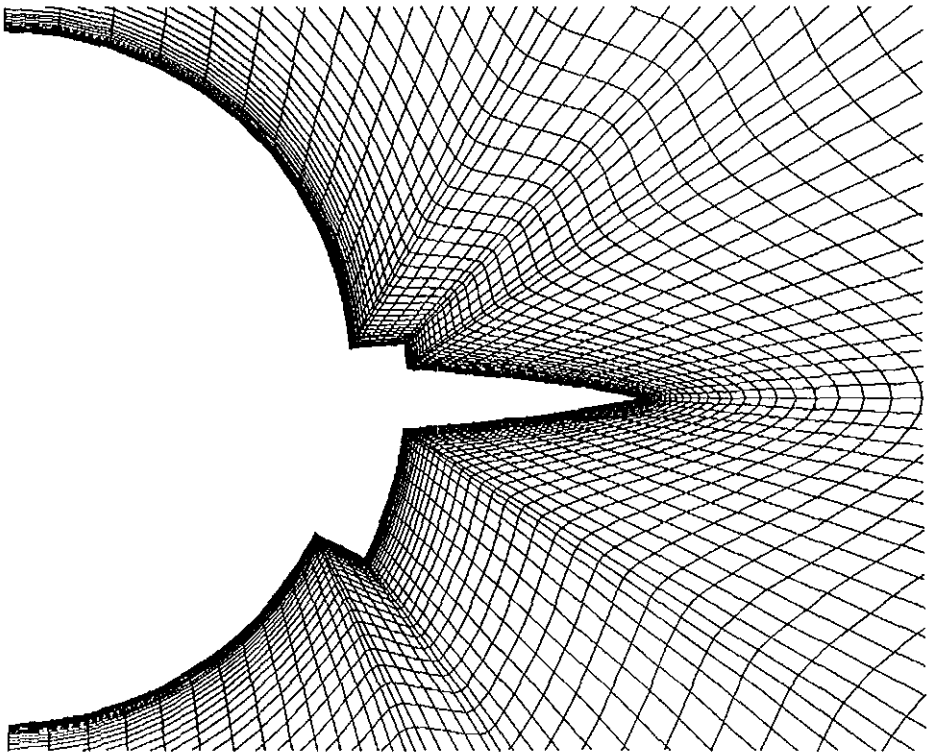

Figure 4.- A typical accelerator crossflow grid.

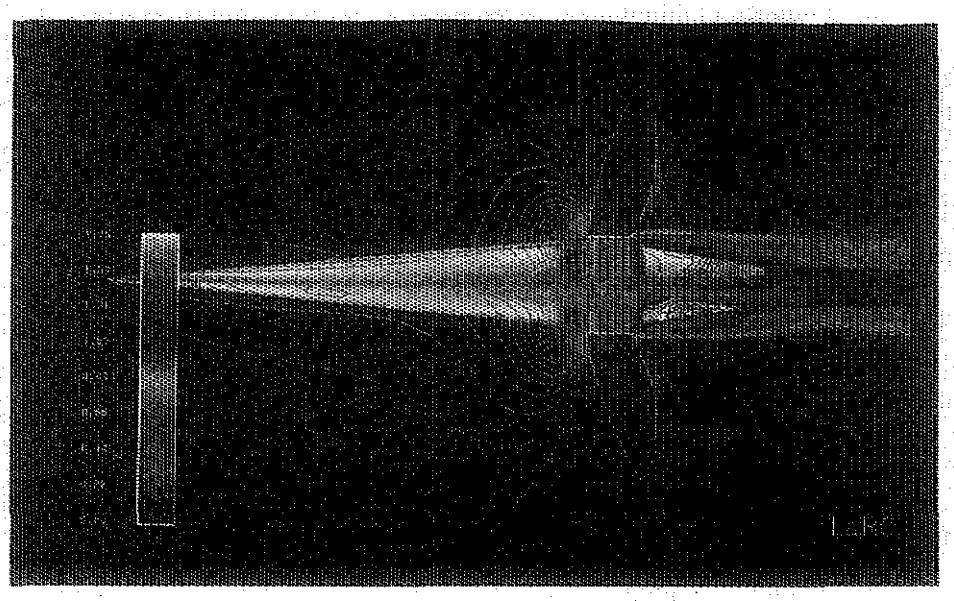

Figure 5.- Surface and plane of symmetry Mach contours.
$M_\infty = 0.9, R_\ell \approx 30 \times 10^6, \alpha = 2°$.

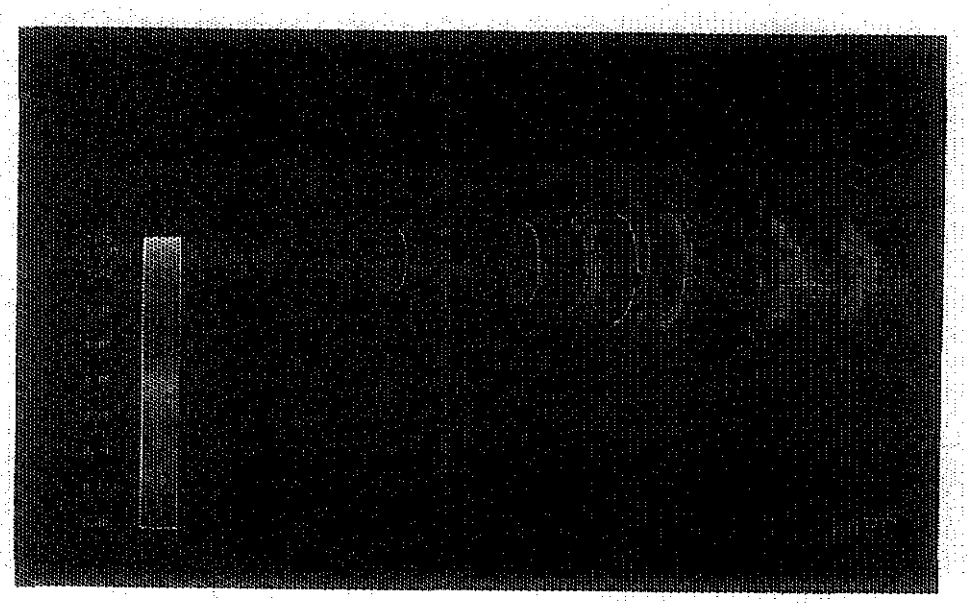

Figure 6.- Mach contours in cross-flow planes. $M_\infty = 0.9, R_\ell \approx 30 \times 10^6, \alpha = 2°$.

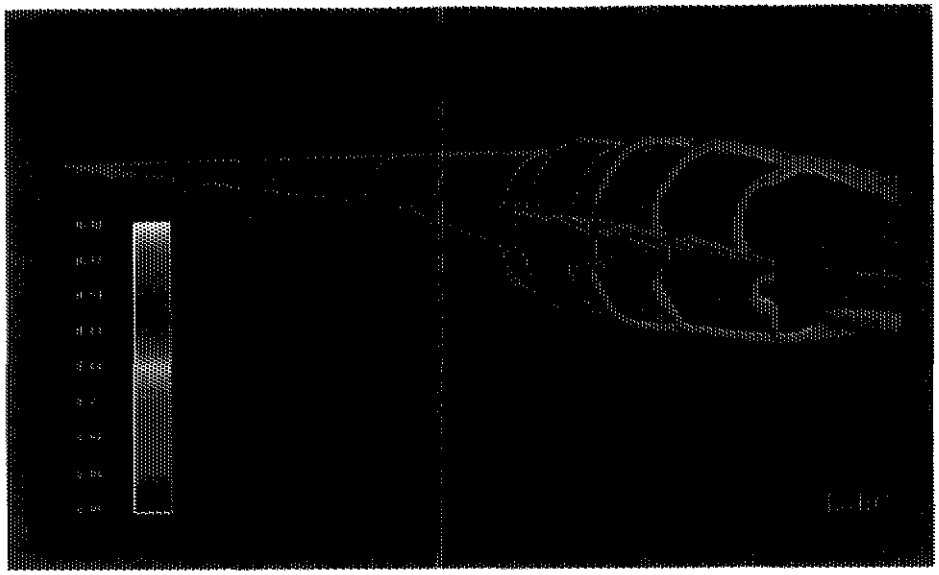

Figure 7(a).- Total pressure contours in crossflow and plane of symmetry - overall view. $M_\infty = 0.9, R_\ell \approx 30 \times 10^6, \alpha = 2^\circ$.

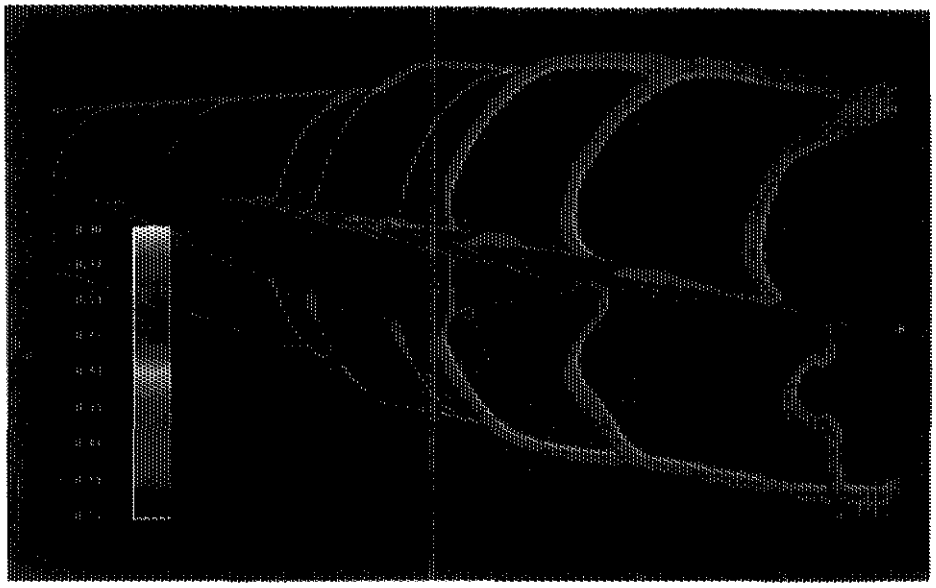

Figure 7(b).- Total pressure contours in crossflow and plane of symmetry - closeup view. $M_\infty = 0.9, R_\ell \approx 30 \times 10^6, \alpha = 2^\circ$.

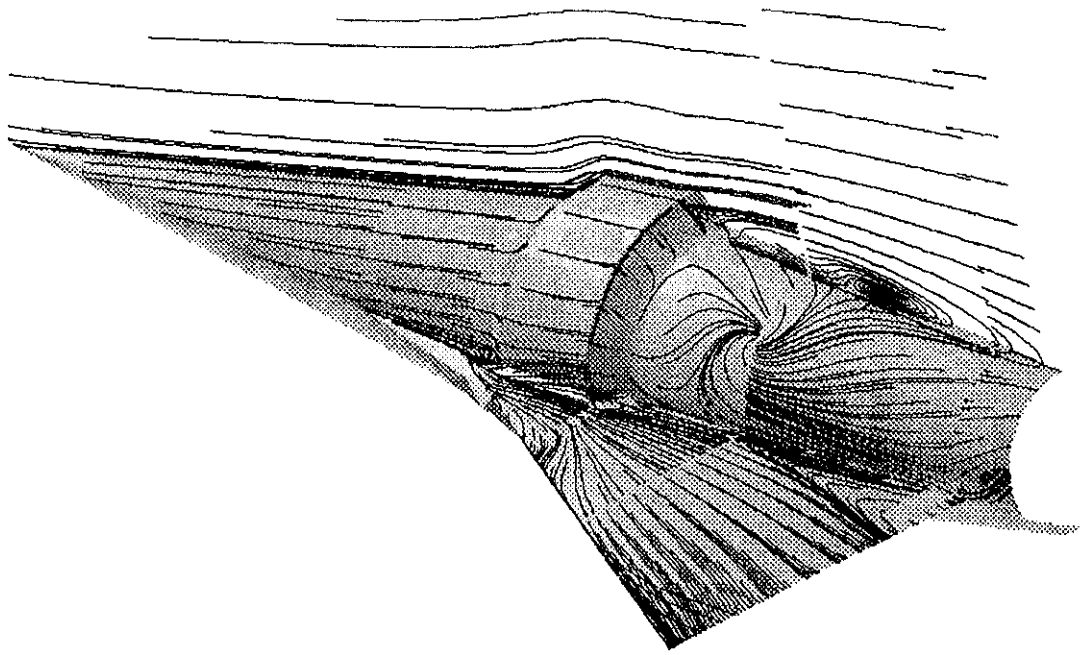

Figure 8.- Streamline pattern on the surface and plane of symmetry.
$M_\infty = 0.9, R_\ell \approx 30 \times 10^6, \alpha = 2°$.

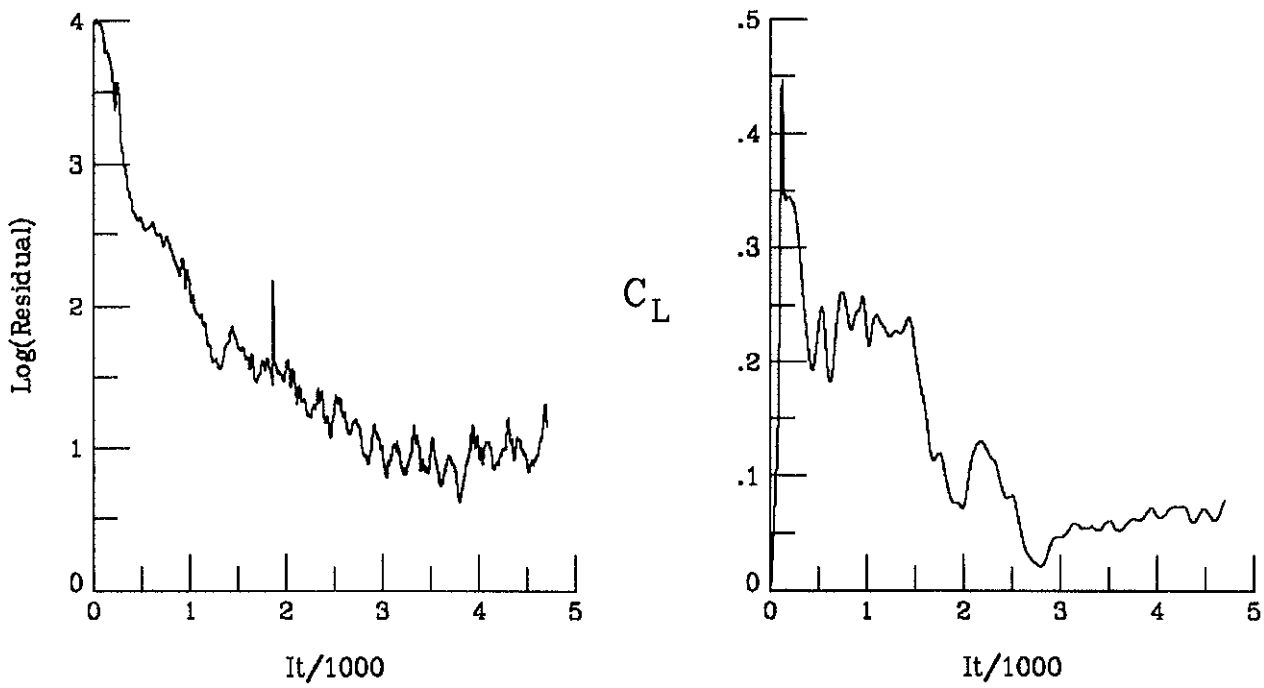

Figure 9.- Overall convergence history. $M_\infty = 0.9, R_\ell \approx 30 \times 10^6, \alpha = 2°$.

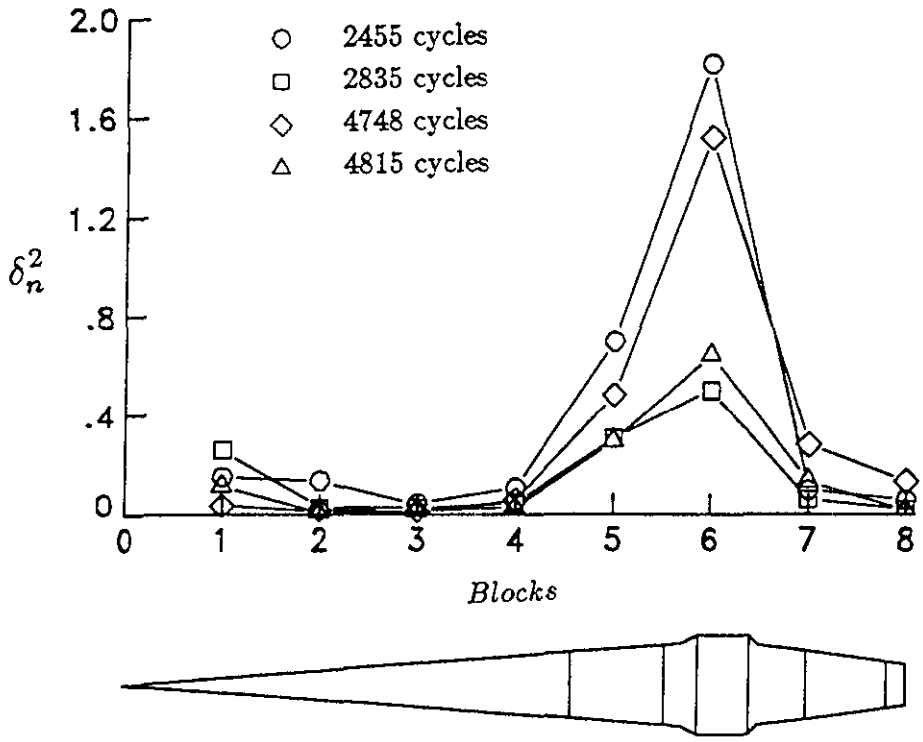

Figure 10.- Block residual history. $M_\infty = 0.9, R_\ell \approx 30 \times 10^6, \alpha = 2°$.

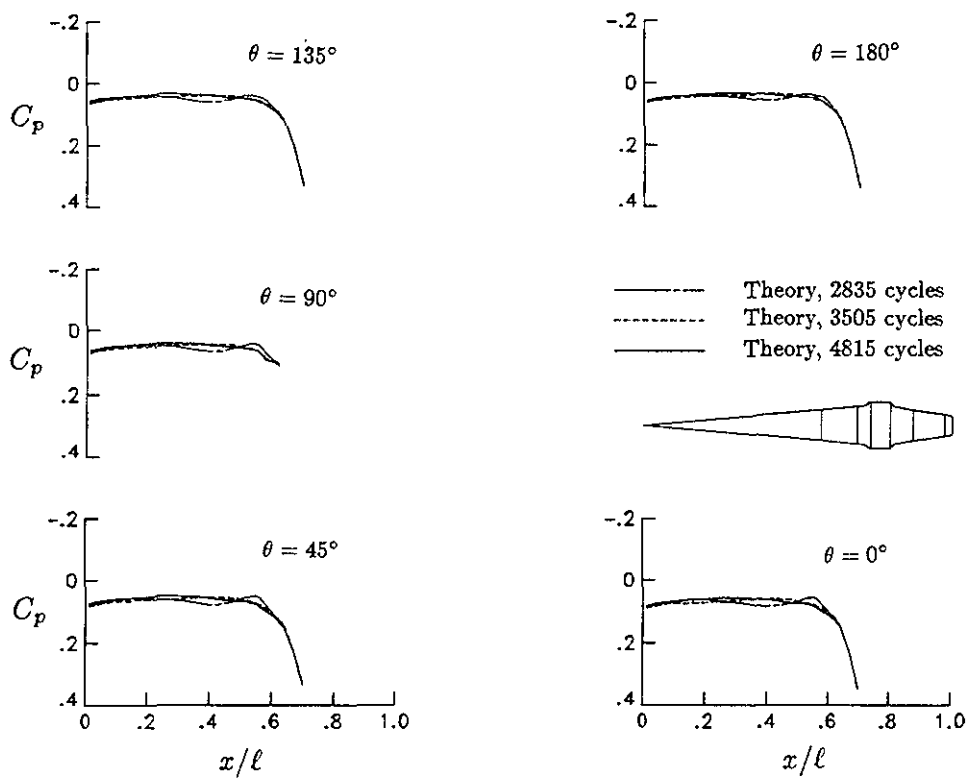

Figure 11.- Forebody surface pressure sensitivity on solution development. $M_\infty = 0.9, R_\ell \approx 30 \times 10^6, \alpha = 2°$.

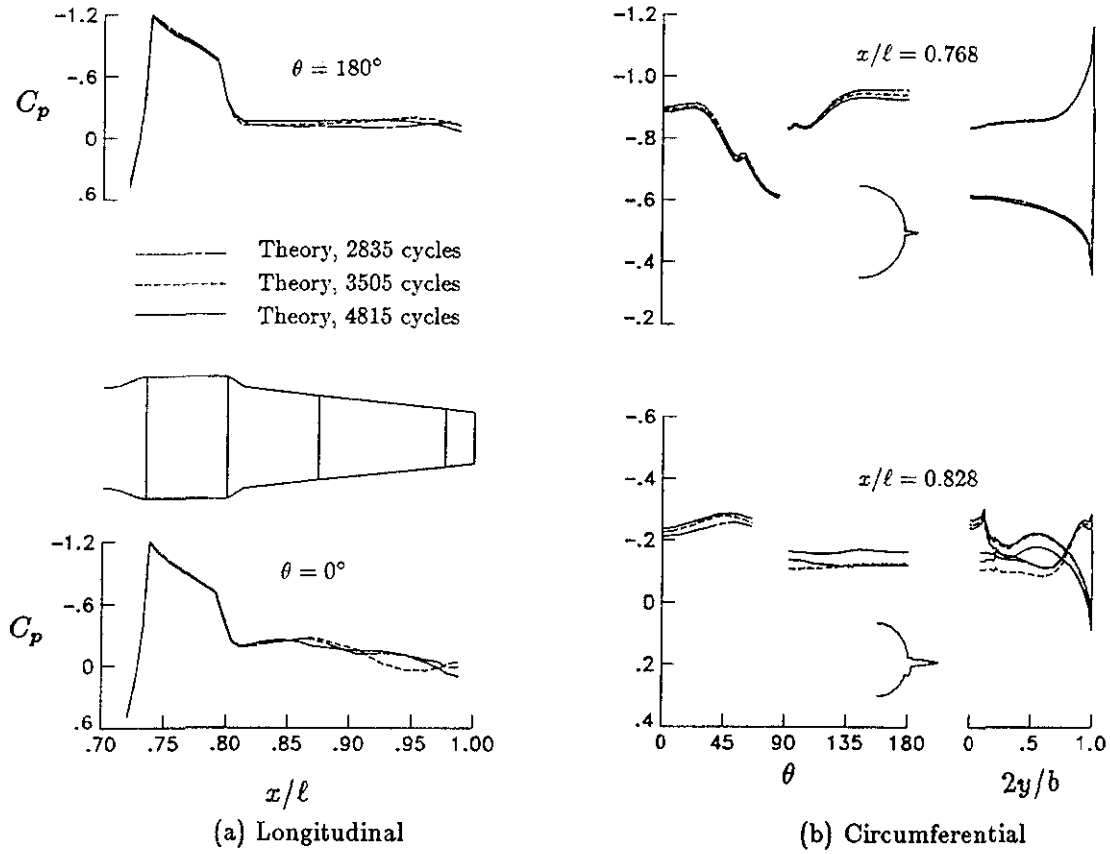

(a) Longitudinal (b) Circumferential

Figure 12.- Boattail surface pressure sensitivity on solution development. $M_\infty = 0.9$, $R_\ell \approx 30 \times 10^6$, $\alpha = 2°$.

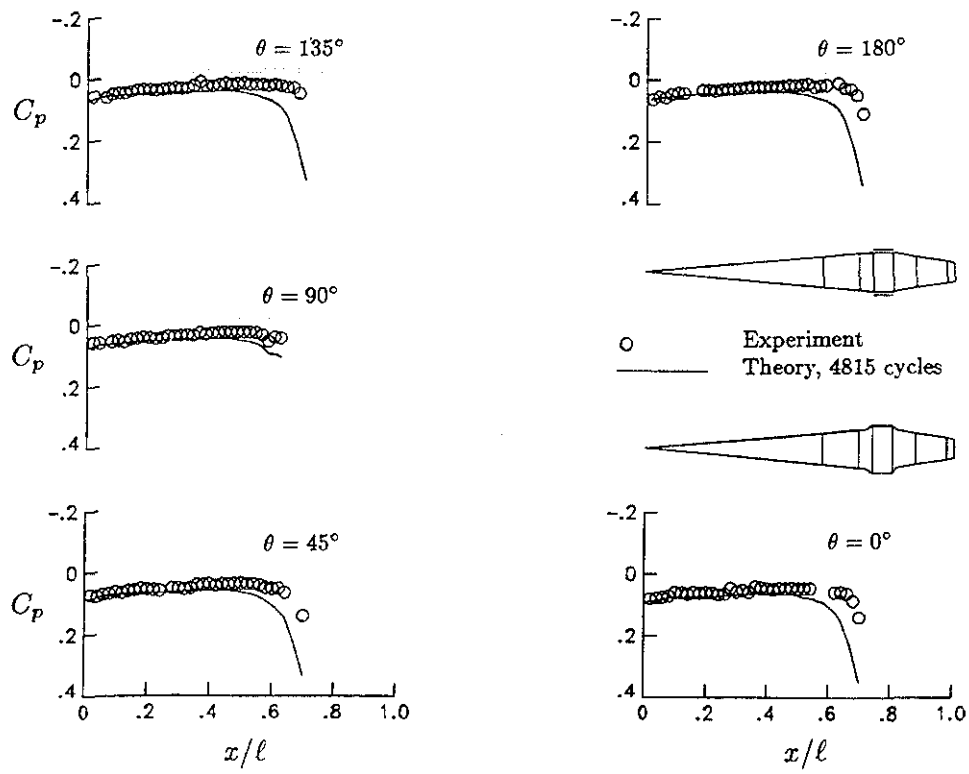

Figure 13.- Forebody surface pressure correlations with experiment. $M_\infty = 0.9$, $R_\ell \approx 30 \times 10^6$, $\alpha = 2°$.

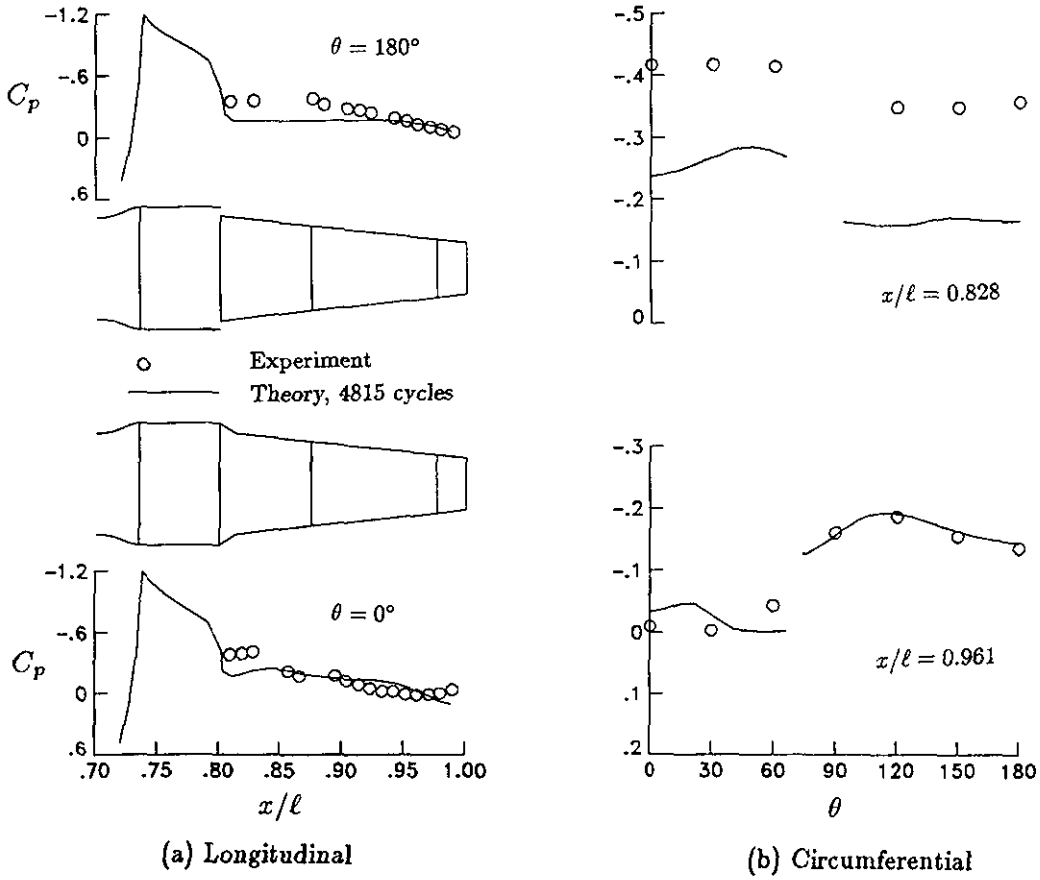

(a) Longitudinal

(b) Circumferential

Figure 14.- Boattail surface pressure correlations with experiment. $M_\infty = 0.9, R_\ell \approx 30 \times 10^6, \alpha = 2°$.